CHAPTER 5 RESULTS AND DISCUSSION

5.1 Physical properties of raw materials

5.1.1 Commercial grade raw materials

Chemical compositions of the commercial grade raw materials are shown in Table 5.1.

Table 5.1 The chemical compositions (weight %) of commercial grade raw materials

Oxide	Al_2O_3	Na_2O	SiO_2	CaO	MgO	K_2O	Fe_2O_3	TiO_2	H_2O	L.O.I.
Alumina A-21	99.78	0.40	0.03	-	-	-	0.03	-	0.50	0.15
Kaolin	22.55	0.41	66.05	0.08	0.54	4.19	0.68	0.02	-	4.65
Ball Clay	23.00	0.22	51.50	0.37	0.12	0.92	1.42	0.63	-	19.60
Talc	0.30	-	58.00	1.10	30.00	-	0.15	-	-	10.00
Spodumene	26.00	0.20	65.00	-	-	7.30	0.06	0.15	-	-

X-ray diffraction pattern of alumina A-21 in Figure 5.1 shows corundum phase.

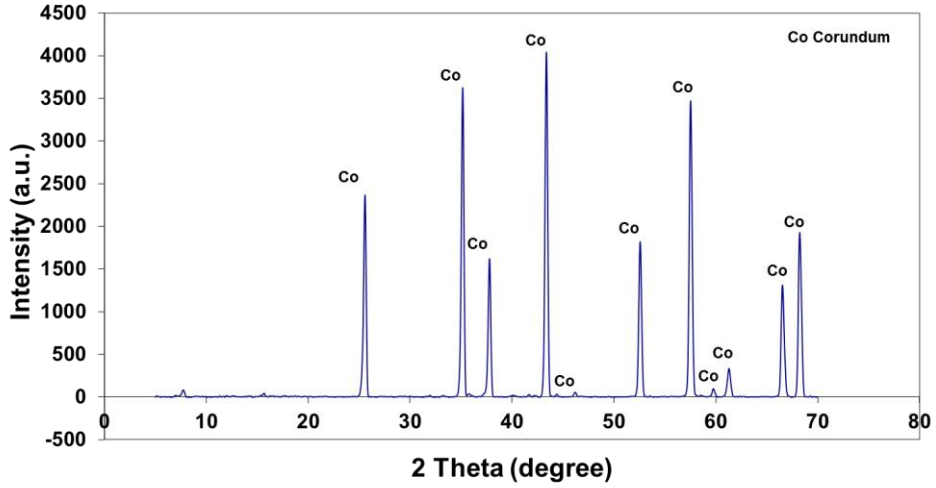

Figure 5.1 XRD pattern of alumina A-21 and the standard peak positions of corundum (Co).

X-ray diffraction pattern of kaolin in the Figure 5.2 shows phases of Kaolinite, Halloysite, Illite, Quartz and Microcline.

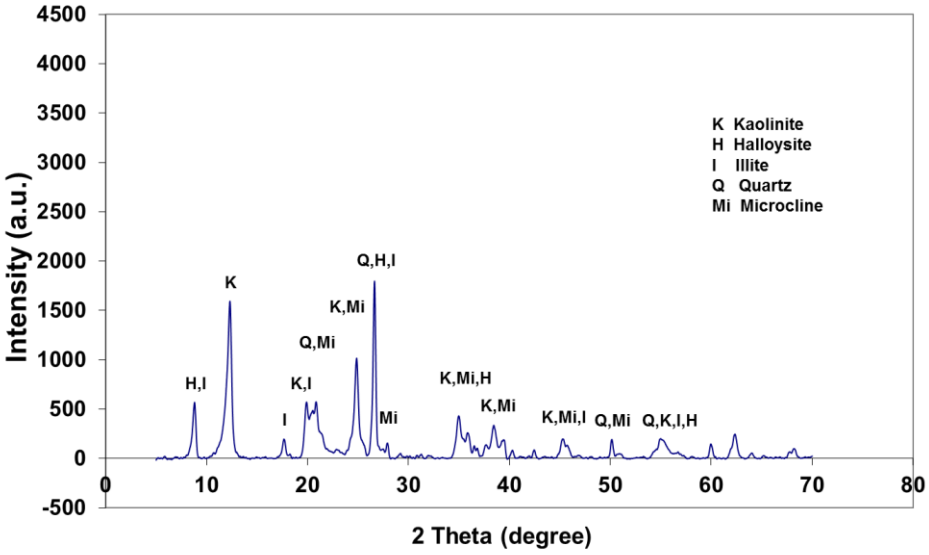

Figure 5.2 XRD pattern of the Kaolin and the standard peak positions of Kaolin (K), Halloysie (H), Illite (I), Quartz (Q) and Microcline (Mi).

X-ray diffraction pattern of ball clay in Figure 5.3 showed phases of Kaolinite, Illite and Quartz.

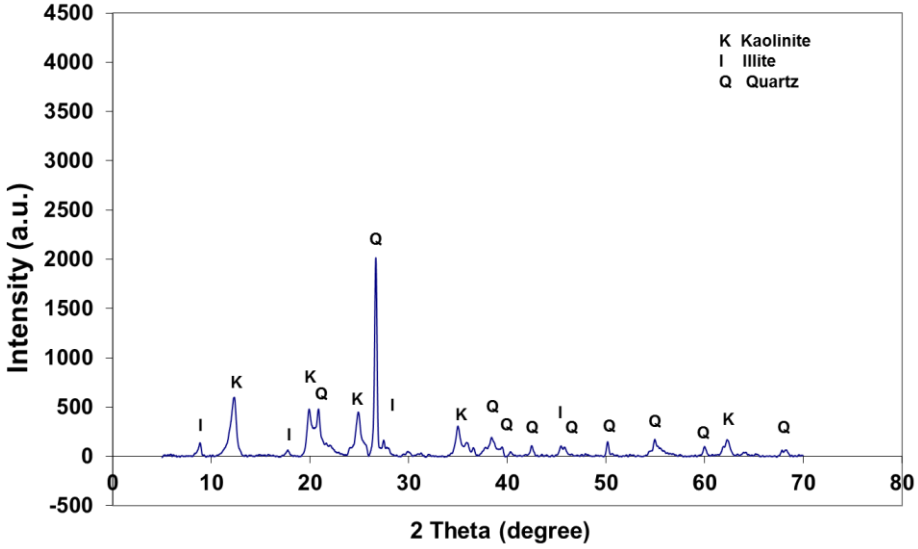

Figure 5.3 XRD pattern of the Ball clay and the standard peak positions of Kaolinite (K), Illite (I) and Quartz (Q).

X-ray diffraction pattern of talc in Figure 5.4 showed phases of Talc, Magnesite, Dolomite and Quartz.

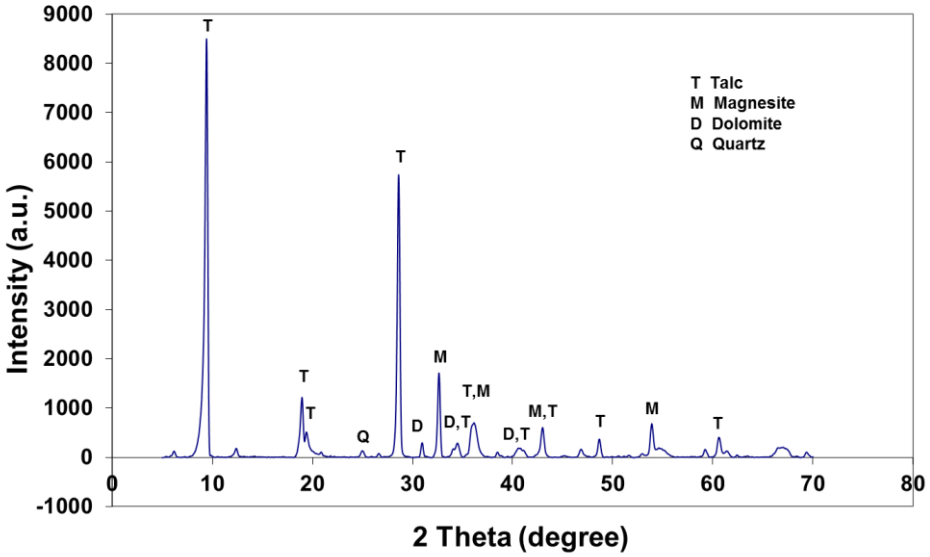

Figure 5.4 XRD pattern of the Talcum and the standard peak positions of talc (T), Magnesite (M), Dolomite (D) and Quartz (Q).

Median particle size and calculated specific surface area of the raw materials are shown in the Table 5.2

Table 5.2 Median particle size (D50) and the specific surface area of commercial raw materials

Raw material	**D50 (µm)**	**Specific Surface Area (m^2/g)**
Alumina	13.27	1.08
Kaolin	8.07	1.81
Ball clay	6.21	2.32
Talcum	46.66	0.17

5.1.2 The industry-waste raw materials

Chemical compositions of the industry-waste raw materials are shown in Table 5.3

Table 5.3 Chemical compositions (weight %) of the industry-waste raw materials

Oxide	**Al_2O_3**	**SiO_2**	**CaO**	**MgO**	**Na_2O**	**K_2O**	**Fe_2O_3**	**TiO_2**	**ZnO**	**L.O.I.**
Aw	78.80	5.42	1.73	4.21	1.08	-	2.68	-	1.63	-
rice husk ash	22.55	66.05	0.08	0.54	0.41	4.19	0.68	0.02	-	4.65

X-ray diffraction pattern of rice husk ash in Figure 5.5 shows phases of Tridymite and Cristobalite.

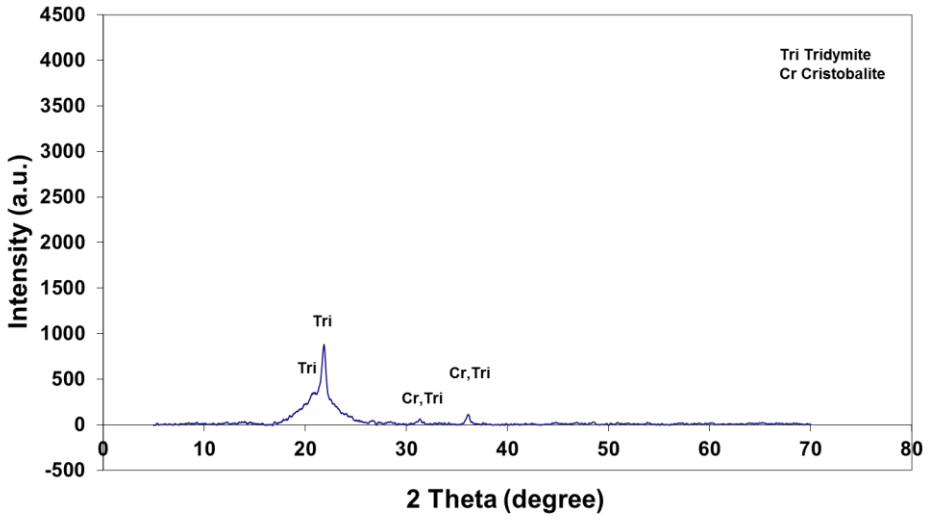

Figure 5.5 XRD pattern of the rice husk ash and the standard peak positions of Tridymite (Tri), and Cristobalite (Cr).

X-ray diffraction patterns of the sludge cake from aluminum scrap and dross recycling industry in Figure 5.6 shows phases of Aluminum oxide, Aluminum magnesium oxide, Potassium aluminum oxide and Corundum.

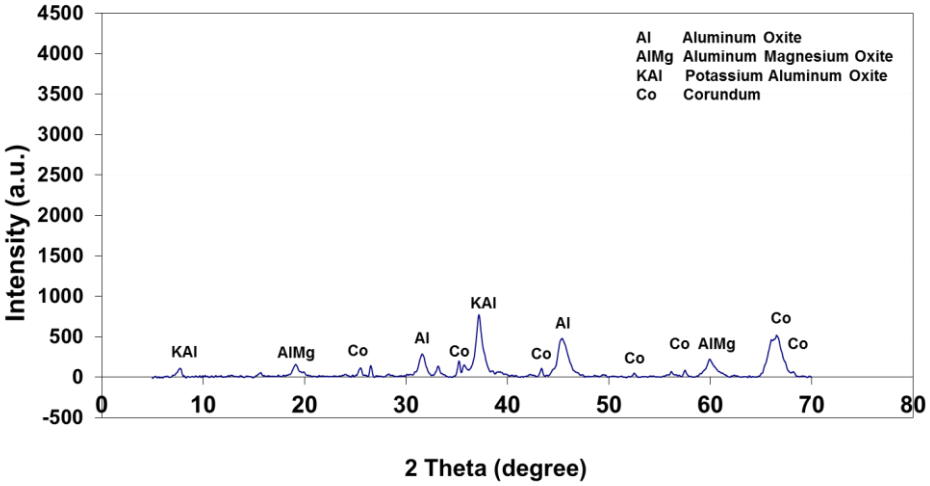

Figure 5.6 XRD pattern of the sludge cake from aluminum scrap and dross recycling industry (Aw) and the standard peak positions of Aluminum oxide (Al), Aluminum magnesium oxide (AlMg), Potassium aluminum oxide (KAl) and Corundum (Co).

Median particle size and calculated specific surface area of the industry wastes, after 5 hours ball milling, are shown in Table 5.4 and Figure 5.7.

Table 5.4 Median particle size (D50) and specific surface area of the industry-waste raw materials

Raw material	D50 (μm)	Specific Surface Area (m^2/g)
Rice husk ash	6.61	1.57
Al sludge waste	23.10	1.68

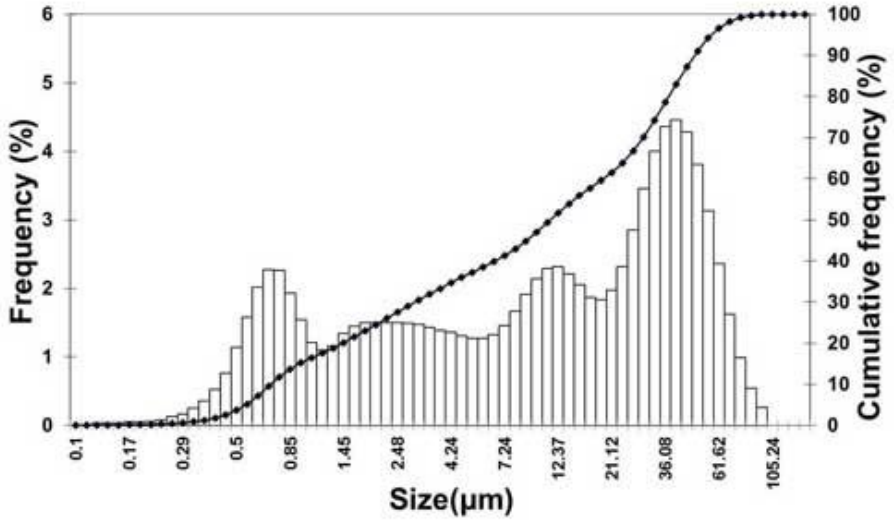

Figure 5.7 Particle size distributions of Aw

5.2 Physical properties and phases of cordierite clay bodies and prototypes from commercial raw materials.

5.2.1 Properties of cordierite clay bodies

1. Thermal shock resistance

Figure 5.8 shows that samples 1, 2, and 3 were intact beyond 290°C which were categorized, in accordance with JIS S 2400, as direct fire high heat- resistance class. On the other hand, samples 4 – 9 were intact beyond 190°C and thus were categorized as direct-fire class.

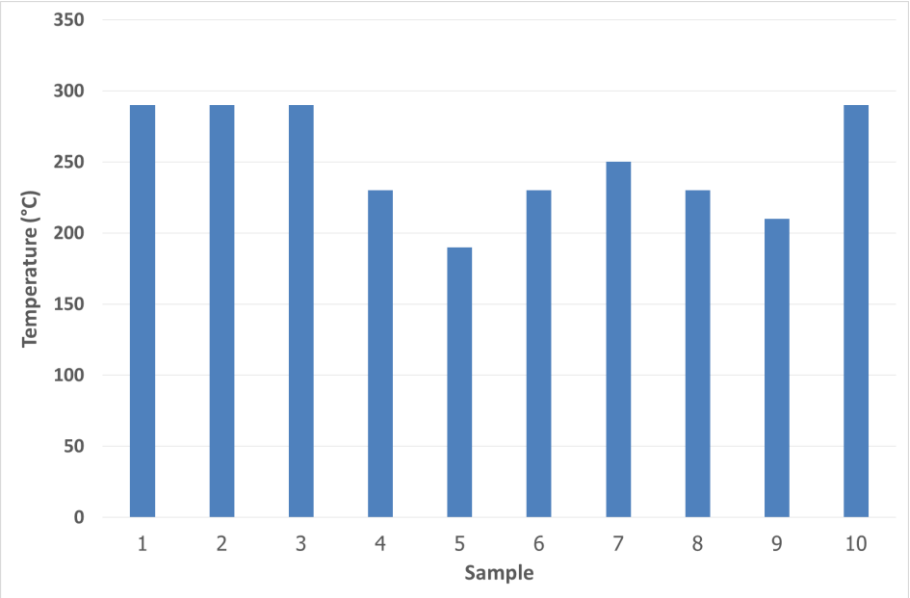

Figure 5.8 Thermal shock resistances of samples after firing at 1250°C.

2. Linear firing shrinkage

Figure 5.9 displays linear firing shrinkage values of samples. The shrinkage values of samples 1, 2, and 3(4.75-6.75 % ± 0.2) were lower than the rest (10.00-16.50 % ± 0.2).

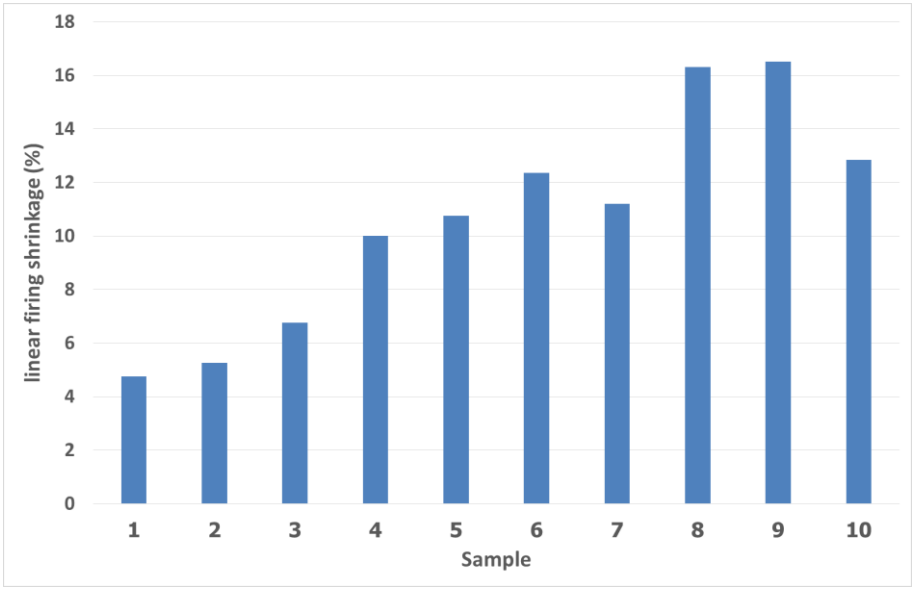

Figure 5.9 The linear firing shrinkage of samples after firing at 1250°C.

3. Water Absorption

In figure 5.10, water absorptions of the samples 7, 8, and 9 were less than 0.2%. Sample 5 had the lowest water absorption value of 0.69%, whereas those of samples 1, 2, 3, 4, and 6 were more than 3%.

The samples with high water absorption values tended to have low linear shrinkage which suggested high porosity. Hence, the samples tended to be more refractoriness than the others.

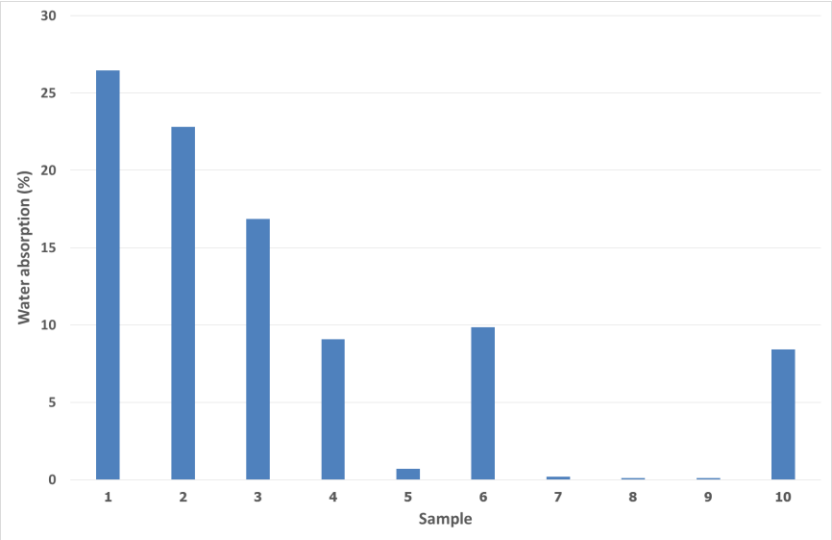

Figure 5.10 The water absorptions of samples after firing at 1250°C.

Samples 1, 2, 3, and 10 which could stand thermal shock resistance more than 290°C had higher values of water absorption than those of samples 7, 8 and 9 with lower thermal shock resistance. Figure 5.11 informs that thermal shock resistance increased with the increasing of porosity. Amount of porosity, generally, reflects the ability to absorb water; the higher the porosity, the greater is the water absorption. Hence, the increasing of thermal shock resistance with the increasing of water absorption observed in this study was in accordance with the relationships shown in Figure 5.11. Moreover, Figure 5.11 shows that resistance to thermal shock is rising again even though there is no further change in porosity. The relationships imply that, at least, there is another factor that affects thermal shock resistance. Findings in the next section may help for an explanation.

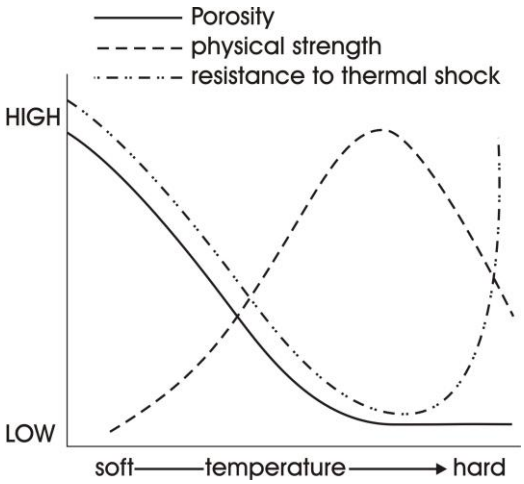

Figure 5.11 Porosity, physical strength and resistance to thermal shock resistance temperature relationships [7]

4. Phases of the cordierite clay bodies

As the product requirement stated so that the ovenware ceramics must have high thermal shock resistance and low water absorption, samples with high thermal shock resistance (no.1, 2, 3, and 10) and those with low water absorption properties (no.7, 8, and 9) were selected for crystal structure investigation. Phases of the samples observed were Cordierite (C), Corundum (Co), Spinel (Sp), and Cristobalite (Cr) as shown in Figure 5.12. Samples 3, 7, and 8 were the first 3 samples with relatively large amount of cordierite, which, theoretically, is necessary for ovenware ceramics.

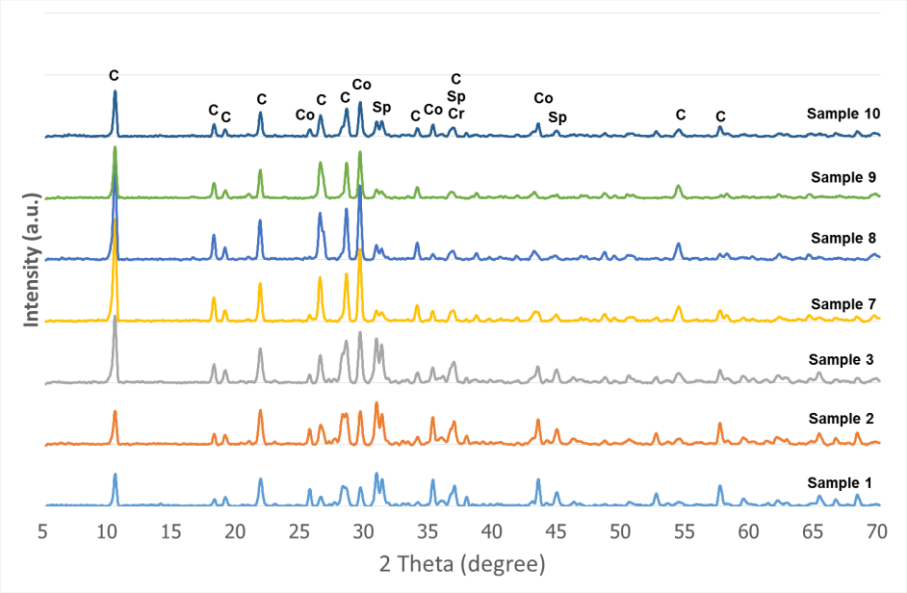

Figure 5.12 XRD patterns of selected samples after firing at 1250°C and the standard peak positions of Cordierite (C), Corundum (Co), Spinel (Sp), and Cristobalite (Cr)

According to Figure 5.11, the samples with low water absorption or low porosity should result in low thermal shock resistance. This is not the case for samples 7, 8, and 9. Obviously, the presence of cordierite in the three samples implied that, in addition to porosity, cordierite also had an influence on thermal shock resistance of the samples and the effect of cordierite was thought to surpass the effect of porosity.

5. Coefficient of thermal expansion

Sample 3, 7, and 8 were chosen for COE study as they had the preferable high thermal shock resistance, moderate water absorption, and relatively high cordierite content. COE of the samples are shown in Figure 5.13. The COE increased from 4.54 $x10^{-6}$ $^{\circ}C^{-1}$of sample 7 to 5.13 $x10^{-6}$ and 6.31 $x10^{-6}$ $^{\circ}C^{-1}$ of samples 8 and 3, respectively. The order of increasing was coherent with the decreasing of the amount of cordierite in the samples.

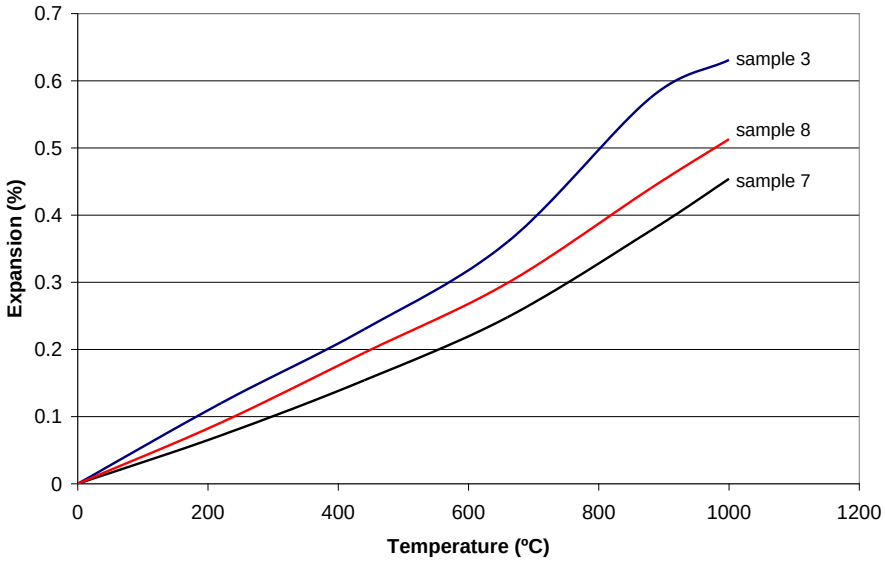

Figure 5.13 COE of samples no. 3, 7and 8

Physical properties of all cordierite clay bodies were summarized in Table 5.5.

Table 5.5 The summary of physical properties of all clay bodies from commercial grade raw materials.

Sample no.	Shock Resistance °C	Water Absorption (%)	Firing Shrinkage (%)	XRD Intensity (2θ ≅ 10.41°)	COE ($x10^{-6}$ °C^{-1})
1	290	26.47	4.75	71.71	-
2	290	22.80	5.25	80.10	-
3	290	16.85	6.75	162.02	6.31
4	230	9.07	10.00	-	-
5	190	0.69	10.75	-	-
6	230	9.85	12.35	-	-
7	250	0.19	11.20	235.45	4.54
8	230	0.10	16.30	228.99	5.13
9	210	0.07	16.50	116.67	-
10	290	8.41	12.85	-	5.71.

All the results led to a conclusion that the formulation of sample 7 was promising with the lowest COE, low water absorption, high cordierite content, and high thermal shock temperature. It was also deduced that more amount of synthesized cordierite should increase thermal shock resistance of the firing clay body. Formulation of sample 7 was thus selected for further grinding to optimize its thermal shock resistance property by varying ball milling time.

5.2.2 Properties of the prototype1

Sample no.7 was selected for the effect of ball milling time on synthesis efficiency of cordierite study. Figure 5.14 shows thermal shock resistance temperatures of samples of different ball milling time. Samples S7-1 and S7-2 were intact above 270°C and the

samples S7-3 to S7-6 were above 250°C. Thermal shock resistance temperature decreased with increasing ball milling time.

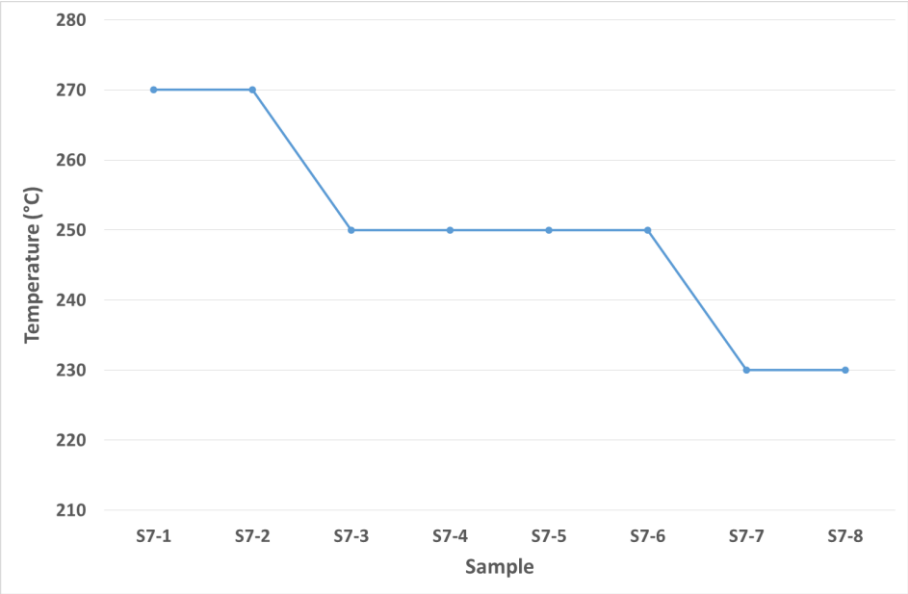

Figure 5.14 Thermal shock resistances of all samples after firing at 1250°C.

Figure 5.15 shows linear firing shrinkage of all samples. Linear firing shrinkage tentatively increased as the ball milling time increased.

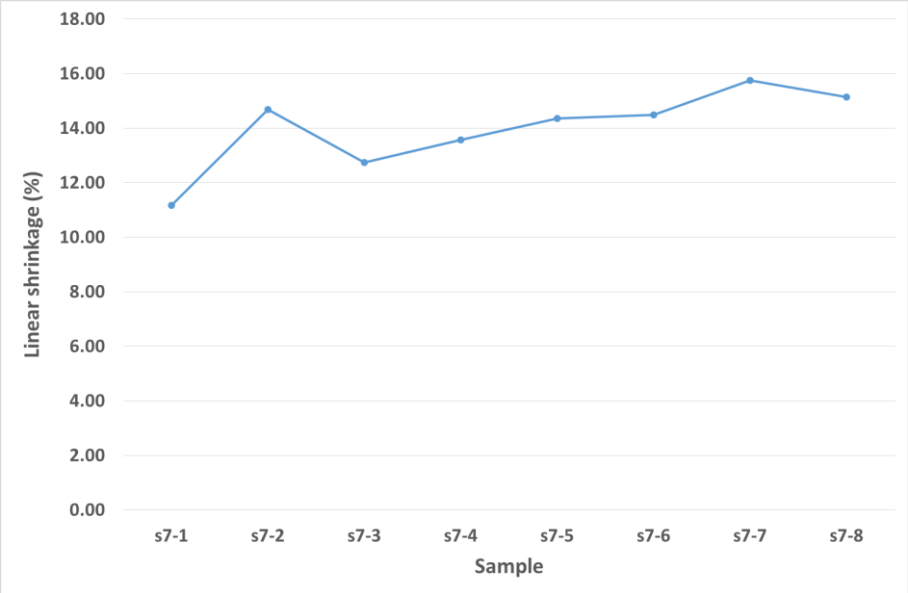

Figure 5.15 Linear firing shrinkage of all prototype1 samples

Figure 5.16 presents that the water absorption value decreased as the ball milling time increased. Water absorption values of sample S7-5 to S7-8, as shown in Figure 5.16 were less than 1%. The values of sample S7-3 and S7-4 were between 1-3%, S7-2 was 9%, and S7-1 was 16%. The samples with low linear shrinkage tended to have high water absorption which suggested that they had high porosity and then high thermal

shock resistance or more refractoriness than those with high linear shrinkage in accordance with the relationships shown in Figure 5.11.

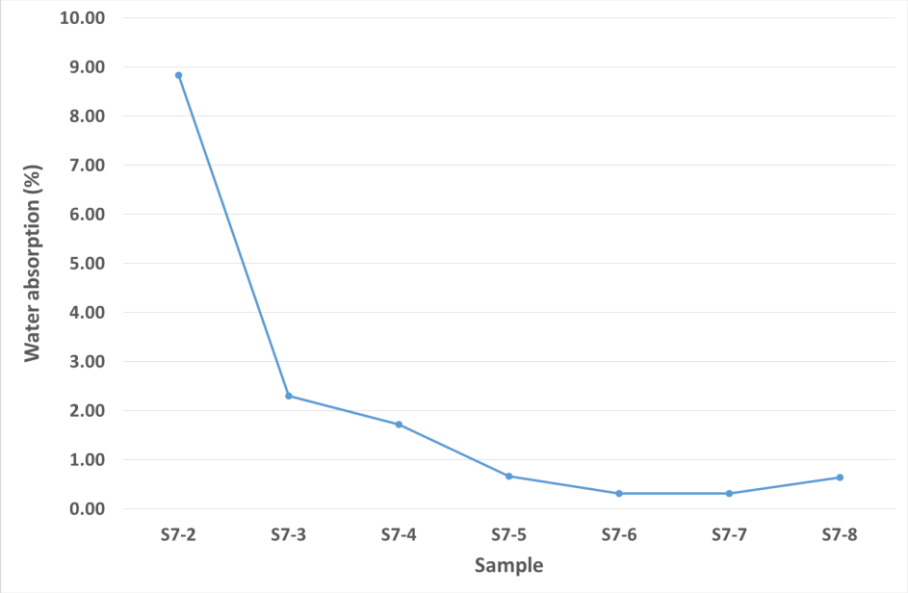

Figure 5.16 Water absorption values of all prototype1 samples.

Phases of all samples in Figure 5.17 were cordierite (C), Corundum (Co), Spinel (Sp), and Cristobalite (Cr). The intensities of cordierite in the samples varied with the ball milling time. The sample S7-6 (5 hours ball milling time) had the highest relative cordierite peak intensity. After a longer milling time than S7-6, samples S7-7 and S7-8 had less relative peak intensity of cordierite than that of S7-6. The results implied that the particle size could only reach a certain size to give reasonable amount of cordierite.

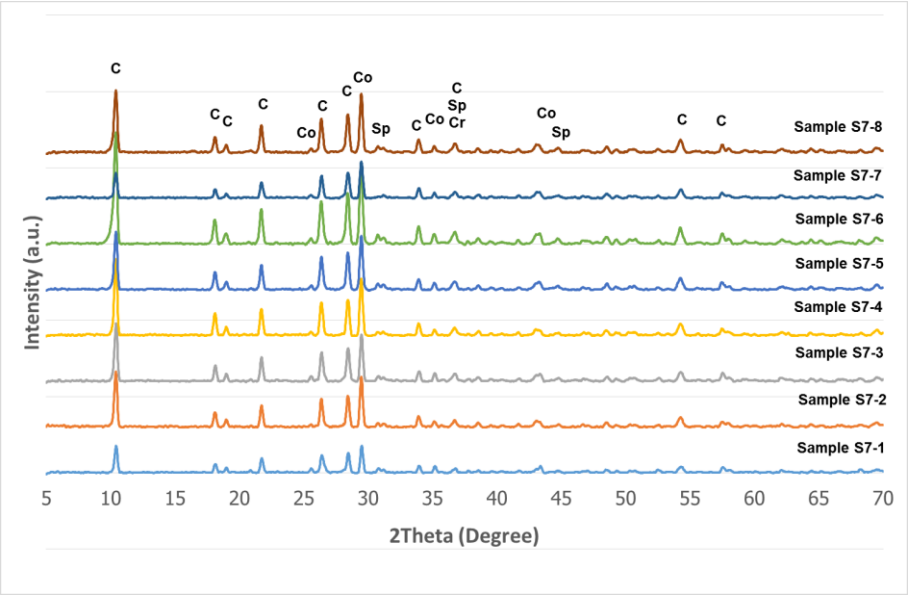

Figure 5.17 XRD patterns of prototype1 samples after firing at 1250°C with the standard peak positions of Cordierite (C), Corundum (Co), Spinel (Sp), and Cristobalite (Cr)

Properties of all prototype1 samples were summarized in Table 5.6.

Table 5.6 Summary of physical properties of all prototype1samples

Sample no.	Shock Resistance °C	Water Absorption (%)	Firing Shrinkage (%)	XRD Intensity (2θ ≅ 10.41°)
S7-1	270	16.01	11.17	175
S7-2	270	8.83	14.68	364
S7-3	250	2.31	12.74	377
S7-4	250	1.72	13.57	500
S7-5	250	0.66	14.35	382
S7-6	250	0.31	14.48	727
S7-7	230	0.32	15.74	165
S7-8	230	0.63	15.14	408

Sample S7-6 with the highest relative peak intensity of cordierite, the lowest water absorption, high thermal shock resistance, and moderate firing shrinkage was thus selected for further study as prototype2.

5.2.3 Properties of the prototype2

The effect of flux on synthesis efficiency of cordierite of sample S7-6 was studied. Figure 5.18 shows thermal shock resistance temperatures of samples with different amount of spodumene or flux in prototype2 at 1250°C firing temperature. Addition of spodumene in the clay body increased thermal shock resistance temperature up to 290°C which is categorized as direct fire high heat-resistance class.

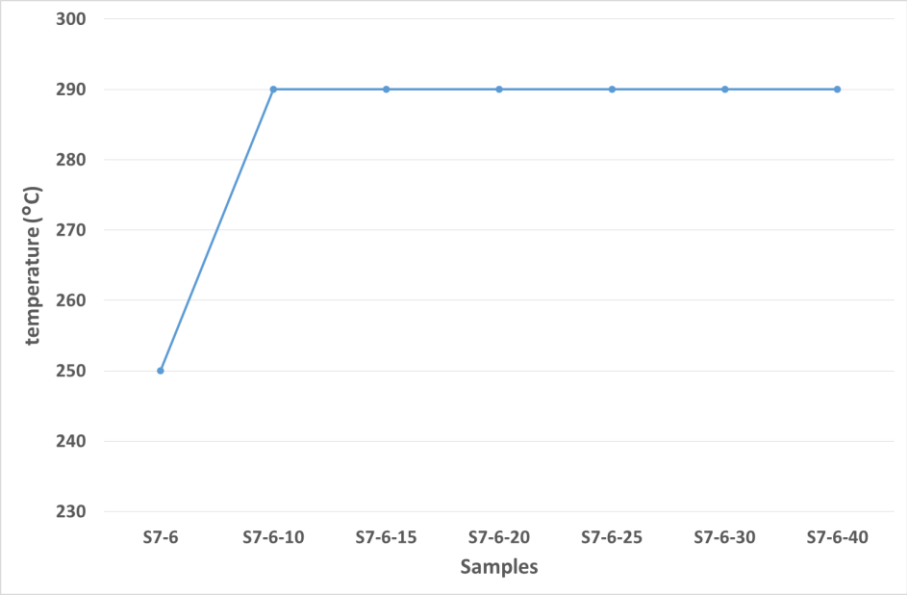

Figure 5.18 Thermal shock resistance of spodumene containing samples after firing at 1250°C.

Figure 5.19 shows linear firing shrinkage of samples after firing at 1250°C. The linear firing shrinkage decreased as the amount of spodumene in the sample increased.

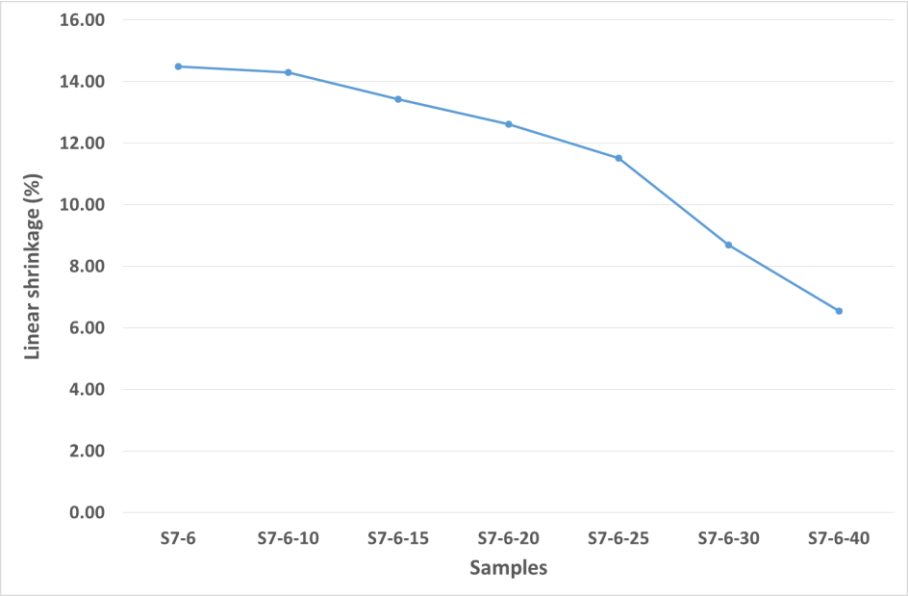

Figure 5.19 The linear firing shrinkage of spodumene containing samples.

Figure 5.20 shows water absorption of the spodumene containing samples sintered at 1250°C. The small amount of spodumene, 10-20%, had no effect on the water absorption. As the amount of spodumene reached 20 %, the water absorption values abruptly increased. Figure.5.19 and Figure 5.20 demonstrated that the samples with low linear firing shrinkage tended to have high water absorption.

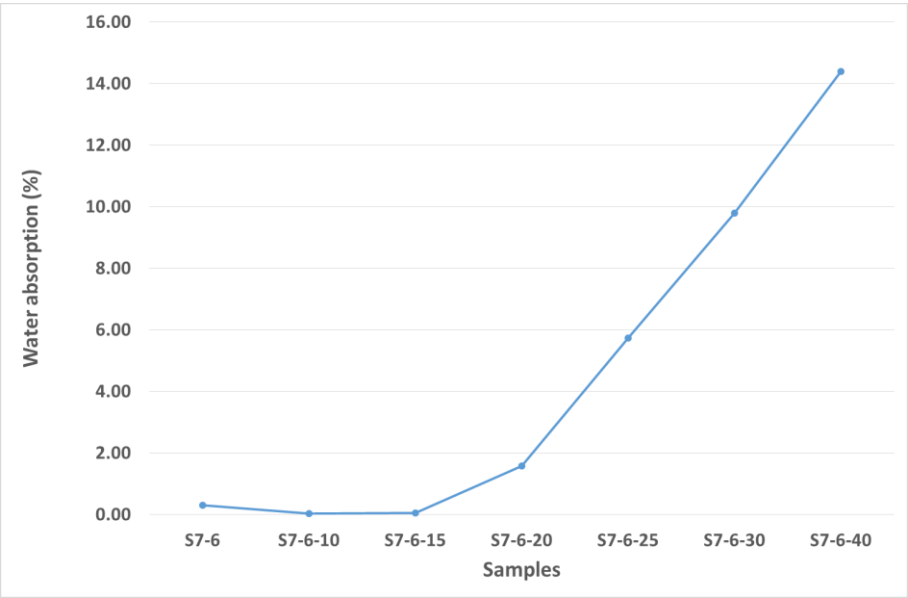

Figure 5.20 The water absorption of spodumene containing samples.

COE values of samples decreased with the increasing amount of spodumene as shown in Figure 5.21. The COE of samples dropped from 4.26×10^{-6} °C^{-1} to 2.89×10^{-6} °C^{-1} as the amount of spodumene increased from 0% to 30%. A slightly decrease of COE was observed for 30% to 40% of spodumene.

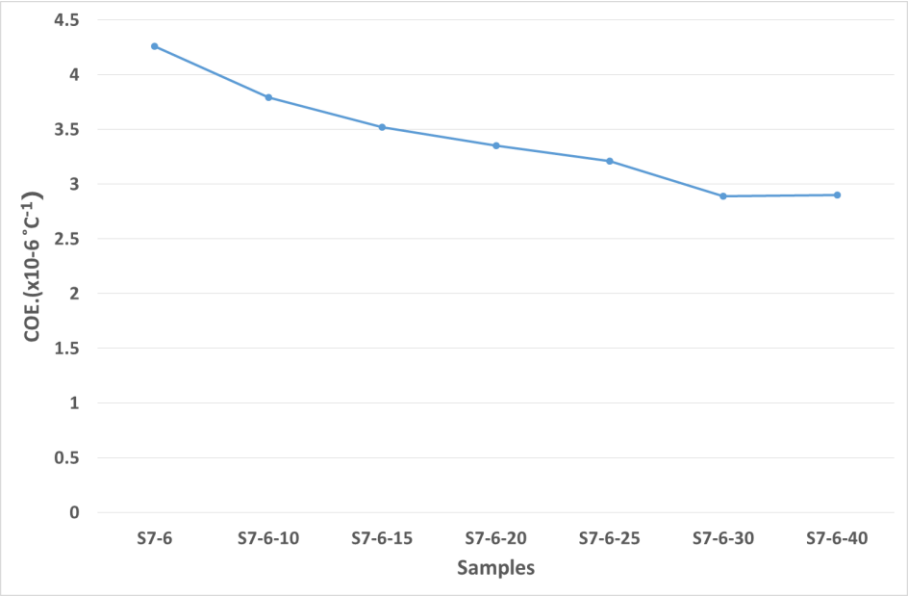

Figure 5.21 COE graph of samples with spodumene adding.

Figure 5.22 depicts x-ray diffraction patterns of the spodumene contaning samples after firing at 1250 °C. Phases of all samples were spodumene (S), cordierite (C), corundum (Co), spinel (Sp), and cristobalite (Cr). The major phases were cordierite and spodumene. The patterns of crystal structure of all samples were the same. Only intensity of sopdumene increased with the increasing amount of spodumene added. The patterns implied that spodumene had no influence on the development of crystal structure. The better thermal shock resistance and lower thermal expansion coefficient values of S7-6 gained after adding spodumene were from the properties of spodumene as reported [27] that spodumene itself has high thermal shock resistance and low thermal expansion coefficient (<0.5 10^{-6} °C^{-1}) [25].

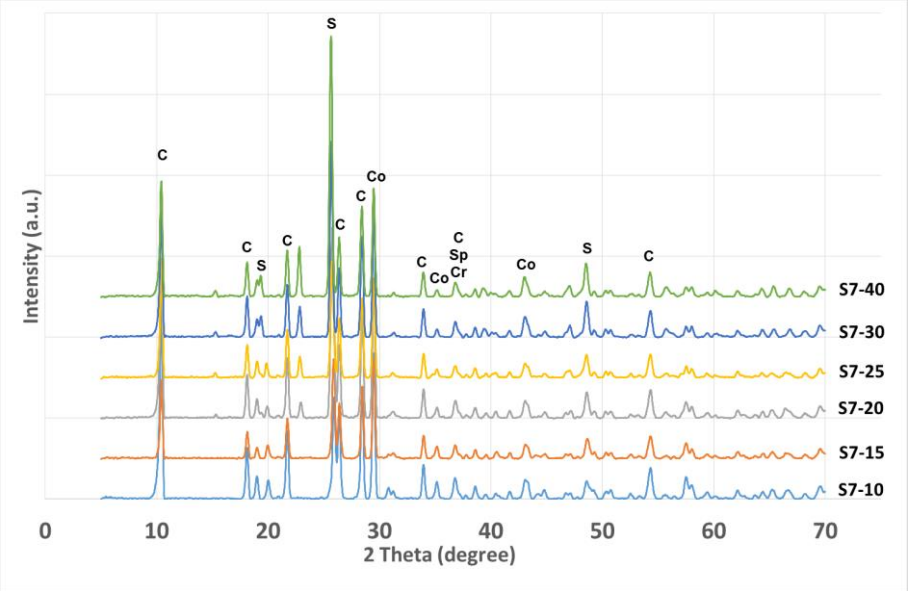

Figure 5.22 XRD patterns of prototype 3 sintered at1250°C with the difference amount of spodumene. The standard peak positions of Spodumene (S), Cordierite (C), Mullite (M), Corundum (Co), Spinel (Sp), and Cristobalite (Cr)

The results mentioned above were summarized in Table 5.7. The properties of available flamewares in market were also presented in the table.

Table 5.7 Summary of physical properties of the S7-6 samples compare with products in market.

Sample no.	Shock Resistance °C	Water Absorption (%)	Firing Shrinkage (%)	COE ($x10^{-6}$ $°C^{-1}$)
S7-6	250	0.31	14.48	4.26
S7-6-10	290	0.03	14.29	3.79
S7-6-15	290	0.05	13.42	3.52
S7-6-20	290	1.58	12.61	3.35
S7-6-25	290	5.74	11.52	3.21
S7-6-30	290	9.97	8.70	2.89
S7-6-40	290	14.39	6.55	2.90
J1*	290	11.79	N/A	1.52
C1*	210	13.91	N/A	4.92

*Data of product from market from chapter 3

Prototype3 was selected with the criteria that the clay body should give a product with high thermal shock resistance, low water absorption, low firing shrinkage, and low COE. In Table 5.7, among all S7-6 samples that satisfied the thermal shock resistance of 290°C, only the samples S7-6-10 and S7-6-15 had the water absorption values within the limit stated by TIS (0.5%). Between the two samples, S7-6-15 had lower firing shrinkage and lower COE than S7-6-10. The clay body S7-6-15 was then selected as prototype3. In comparison with Japanese flameware, ceramics from S7-6-15 showed

comparable thermal shock resistance and better water absorption. It is only inferior in COE. Moreover, in comparison with Chinese flameware, ceramics from S7-6-15 demonstrated better the values of thermal shock resistance, water absorption, and COE value. With such properties, the S7-6-15 clay body can help increase Thai SME capability and competitiveness in ovenware and flameware business. Figure 5.23 depicts a flameware in the form of 8 inch diameter bowl using S7-6-15 clay body.

Figure 5.23 The prototype S7-6-15 after pass thermal shock resistance test at 290˚C for 5 times

5.3 Physical properties and the phase of prototype from waste raw materials

5.3.1. Properties of synthesis bodies using rice husk ash as a new source of SiO_2 (Prototype4)

All firing clay body samples with different sources of SiO_2, quartz (Q), rice husk (R), and commercial clay (C) passed thermal shock resistance at 290°C.

Figure 5.24 shows linear shrinkage values of samples Q, R, and C firing at 1250°C and 1280°C. At both firing temperatures, sample R presented higher shrinkage values than those of Q and C. Table 5.8 presents that particle R had the largest surface area which implied the smallest particle size. The smaller the particle size, the better was the packing. Hence, the particle size of rice husk was responsible for the highest shrinkage of the sample when sintered. However, the shrinkage of R at the 1250°C firing temperature was found to be much lower than that of the sample fired at 1280°C. The reason for this was that firing temperature of 1250°C may not be high enough for particle fusion.

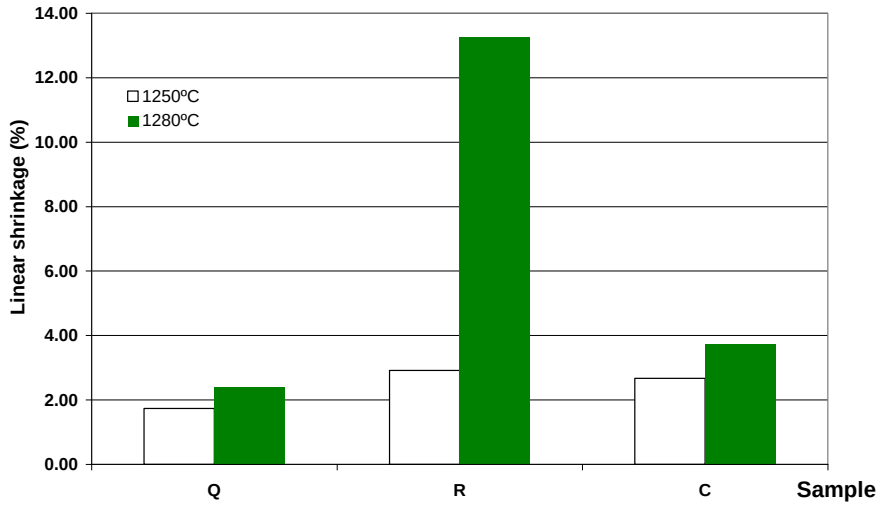

Figure 5.24 Linear firing shrinkage of the samples Q, R, and C after firing at 1250°C and 1280°C.

Table 5.8 Surface areas of particles from different sources

Sample no.	Surface area (m^2/g)
Q	13.7
R	31.3
C	9.78

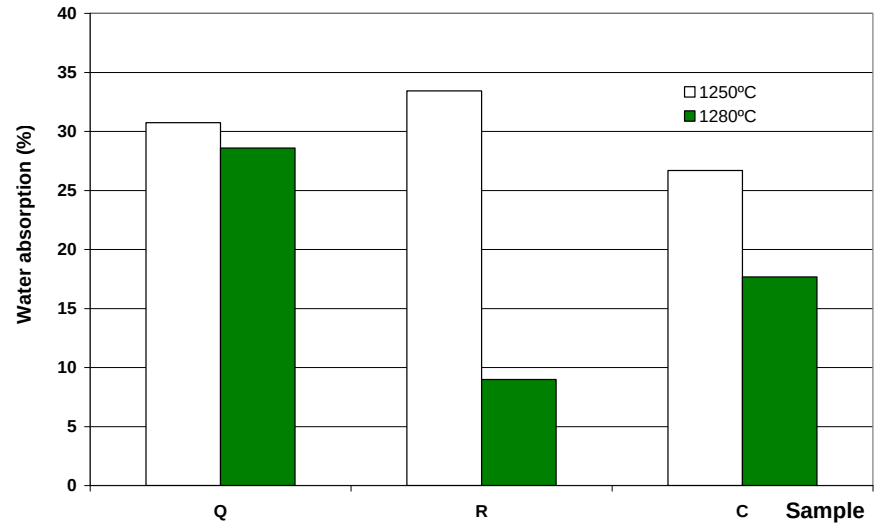

Figure 5.25 The water absorption of the samples Q, R and C after firing at 1250°C and 1280°C**.**

Water absorption values of the sample Q, R, and C at 1250°C and 1280°C are shown in Figure 5.25. At 1250°C firing temperature, sample R had the highest water absorption value of 33.42 %± 0.2. However, at the temperature of 1280°C, sample R gave the lowest value of 8.98 % ± 0.2. At the latter firing temperature, sample R achieved the

best vitrified resulted in the highest shrinkage and the least water absorption. At 1250°C, even though the sample R gave the highest shrinkage, the largest amount of water absorption was observed. The finding was in agreement with the above mentioned explanation for linear shrinkage results of the existence of non-fused particles which resulted in the highest porous body.

Figure 5.26 (a) and (b) shows XRD patterns of all samples fired at 1250°C and 1280 °C. The phases of the samples were found to be cordierite (C), Mullite (M), Corundum (Co), Spinel (Sp), Quartz (Q), Protoenstatite (P) and Cristobalite (Cr). Phase compositions of the samples at different sintering temperature are shown in Table 5.9. For sample C, cordierite was formed at both 1250°C and 1280°C. For samples Q and R, at the same firing temperatures Protoenstatite (MgSiO3) with Corundum and Quartz were formed and no cordierite observed.

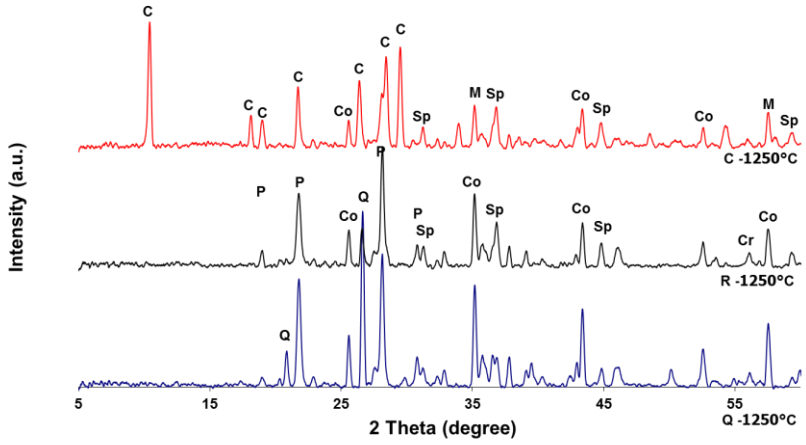

(a)

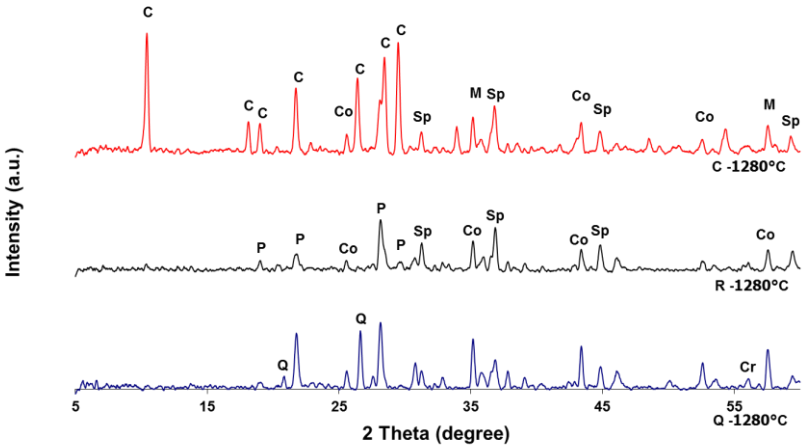

(b)

Figure 5.26 XRD patterns of samples after firing at (a)1250°C and (b) 1280°C with the standard peak positions of Cordierite (C), mullite (M), Corundum (Co), Spinel (Sp), Quartz (Q), Protoenstatite (P) and Cristobalite (Cr)

Generally, cordierite is formed at temperature higher than 1300°C. Hence, the firing temperature of 1300°C was applied for sample Q and R. Figure. 5.27 shows that cordierites were developed for both sample Q and R which could be easily detected at 2θ of 10.41°. At the temperature, the integrated intensity of cordierite for sample R (55.47) was larger than that of sample Q (17.17).

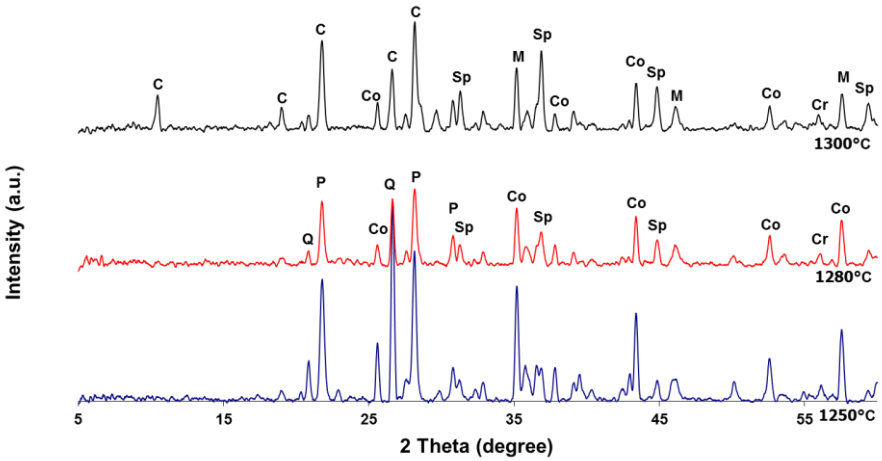

(a)

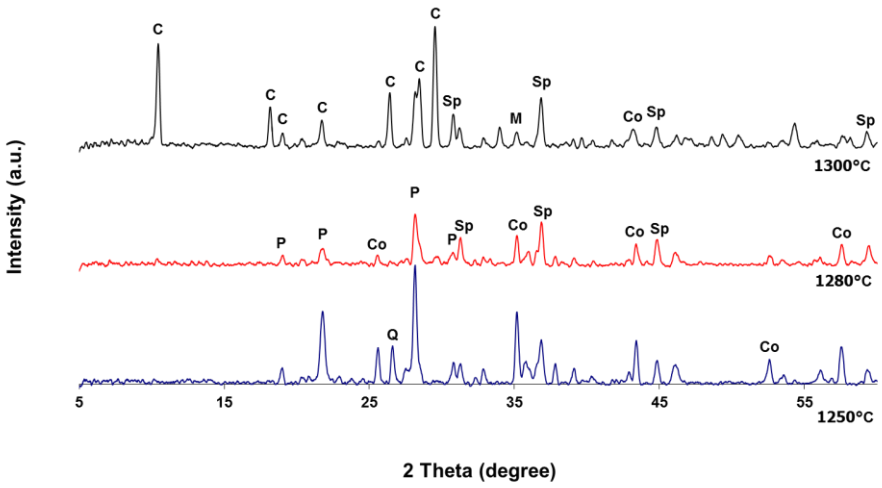

(b)

Figure 5.27 XRD patterns of samples after firing at 1250, 1280 and 1300°C (a) sample Q and (b) sample R with the standard peak positions of Cordierite (C), mullite (M), Corundum (Co), Spinel (Sp), Quartz (Q), Protoenstatite (P) and Cristobalite (Cr)

Table 5.9 XRD results of all samples at different firing temperatures

Sample	Temperature (°C)	Crystalline phase
Q	1250°C	Protoenstatite, Quartz, mullite, Corundum, Spinel, and Cristobalite
	1280°C	Protoenstatite, Quartz, mullite, Corundum, Spinel, and Cristobalite
	1300°C	Cordierite, mullite, Corundum, Spinel, and Cristobalite
R	1250°C	Protoenstatite, Quartz, mullite, Corundum, Spinel, and Cristobalite
	1280°C	Protoenstatite, Quartz, mullite, Corundum, Spinel
	1300°C	Cordierite, mullite, Corundum, Spinel
C	1250°C	Cordierite, mullite, Corundum, Spinel, and Cristobalite
	1280°C	Cordierite, mullite, Corundum, Spinel
	1300°C	N/A

COE values of the Q, R and C samples are shown in Table 5.10 and Figure 5.28. At firing temperature of 1250°C, COE increased in the order of the C, R, and Q. The same increasing order was also observed for those firing at 1280°C.

Table 5.10 COE of all samples at different firing temperatures

Sample no.	1250°C (1 x10^{-6}/°C^{-1})	1280°C (1 x10^{-6}/°C^{-1})
Q	10.20	5.66
R	8.48	7.86
C	5.71	5.31

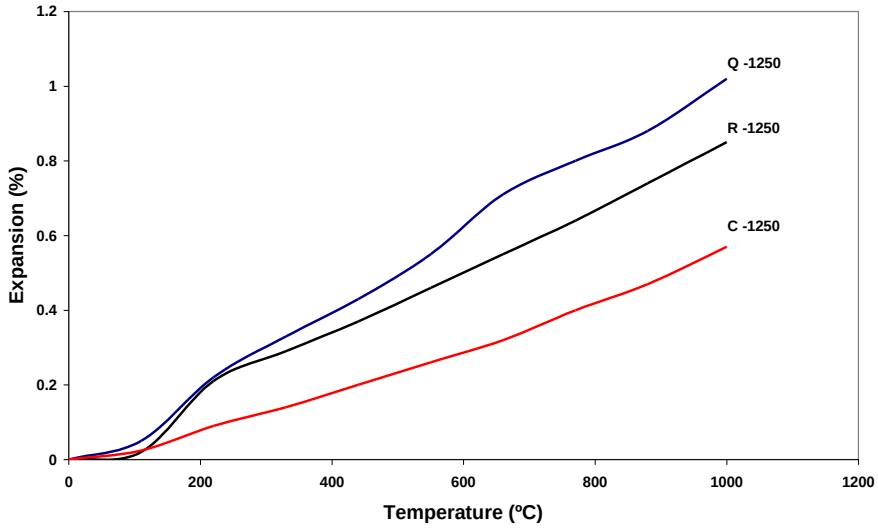

(a)

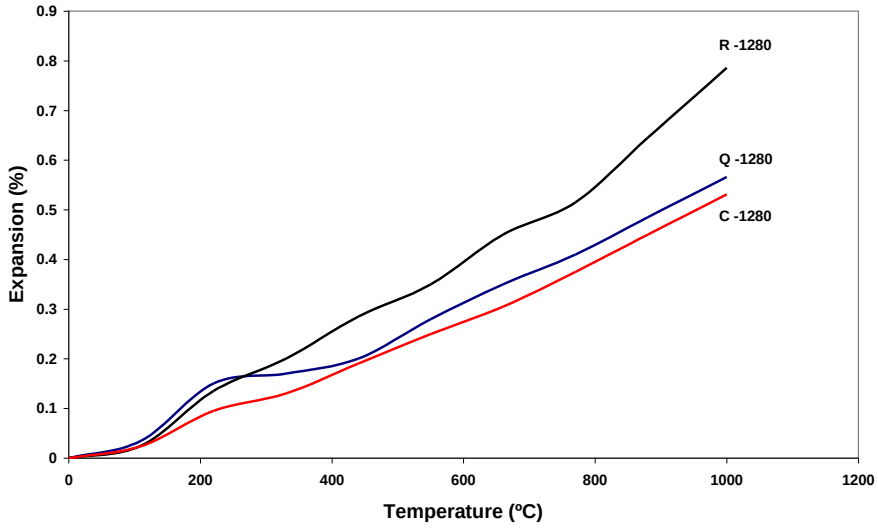

(b)

Figure 5.28 COE graph of sample Q, R and C. at (a) 1250°C and (b) 1280°C

Properties of synthesis bodies Q, R, and C firing at 1250°C and 1280°C are summarized in Table 5.11.

Table 5.11 Summary of physical properties of the samples at (a) 1250°C and (b) 1280°C

(a)

Sample no.	Shock Resistance (°C)	Water Absorption (%)	Firing Shrinkage (%)	Crystalline phase	COE ($x10^{-6}$ °C^{-1})
Q	290	30.73± 0.2	1.73± 0.2	Protoenstatite, Quartz, Mullite, Corundum, Spinel, Cristobalite	10.20
R	290	33.42± 0.2	2.92± 0.2	Protoenstatite, Quartz, Mullite, Corundum, Spinel, Cristobalite	8.48
C	290	26.68± 0.2	2.67± 0.2	Cordierite, Mullite, Corundum, Spinel, Cristobalite	5.71

(b)

Sample no.	Shock Resistance (°C)	Water Absorption (%)	Firing Shrinkage (%)	Crystalline phase	COE ($x10^{-6}$ °C^{-1})
Q	290	28.59± 0.2	2.41± 0.2	Protoenstatite, Quartz, Mullite, Corundum, Spinel, Cristobalite	5.66
R	290	8.98± 0.2	13.25± 0.2	Protoenstatite, Quartz, Mullite, Corundum, Spinel	7.86
C	290	17.67± 0.2	3.73± 0.2	Cordierite, Mullite, Corundum, Spinel	5.31

Table 5.12 The COE values of the materials [20, 19, 28, 6]

Materials	COE. ($\times 10^{-6}$ °C^{-1})
Cordierite	0.8 - 2.0
Mullite	4.0
Alumina	8.9 - 9.0
Spinel	8.0 - 9.0
SiC	4.0
Cristobalite	2.6

The differences of COE of different samples could be explained using equation (1).

$$\alpha_{with} = (\alpha_1 v_1 + \alpha_2 v_{2+} \alpha_3 v_3)(1-P) \quad (1)$$

Coefficient of thermal expansion (COE) of composite materials is α_{with}. Where α_1, α_2 and α_3 are the thermal expansion coefficients of each phase/raw material, v_1, v_2 and v_3 are the volume fractions, and P is the porosity [28]. According to equation (1), sample with phases of low COE values and high porosity would give low COE.

Table 5.12 presents the values of COE of different phases/raw materials. Moreover, in this study, the values of water absorption were used to imply the amount of porosity in comparison. The higher the water absorption, the greater is the amount of porosity.

At 1250°C, the majority of phases observed were the same for samples Q, R, and C which were cristobalite, spinel, corundum, and mullite. The differences were that only sample C had cordierite whereas samples Q and R had quartz and protoenstatite. Even though Table 5.12 presents that cordierite has the lowest COE value, sample C got also the lowest value of water absorption. The latter implied the lowest amount of porosity and thus would affect the overall COE of the sample to the high side. Still, sample C presented the lowest COE value. The effect on COE caused by the presence of cordierite phase was thought to surpass the effect of porosity. The same reason was applicable for the samples firing at 1280°C. Sample C, the only sample with cordierite phase gave the lowest COE even though the water absorption value or the amount of porosity was not the highest.

For the samples Q and R which had no cordierite, the effect of the amount of porosity on COE became apparent. Samples prepared from both the firing temperatures of 1250°C and 1280°C with higher water absorption or greater amount of porosity presented lower values of COE.

In conclusion, sample R or prototype4 was not worth further development because cordierite could only obtained at firing temperature at least 1300°C which was higher than that of commercial clay.

5.3.2. Properties of the synthesis bodies using sludge cake from aluminum scrap and dross recycling industry as a new source of Al_2O_3 (Prototype 5)

All samples of different sources of Al_2O_3, sample W used Al_2O_3 from sludge cake from aluminum scrap and dross recycling industry (Aw) and sample C used commercial Al_2O_3, passed thermal shock resistance test at 290 °C.

Figure 5.29 displayed the linear firing shrinkage of samples W and C. at 1200-1325°C. The W-samples got higher shrinkage values than that of C-samples for all sintering temperatures. The smaller particle size of Aw (The data was shown in chapter 4) as well as CaO, MgO, Fe_2O_3 and ZnO, consisted in Aw functioned as flux allowed the particles to be easily fused and better packing while sintering. For both W and C, the onset temperature for increasing shrinkage was 1225 °C. The values leveled off at 1280 °C and 1250 °C for W and C, respectively.

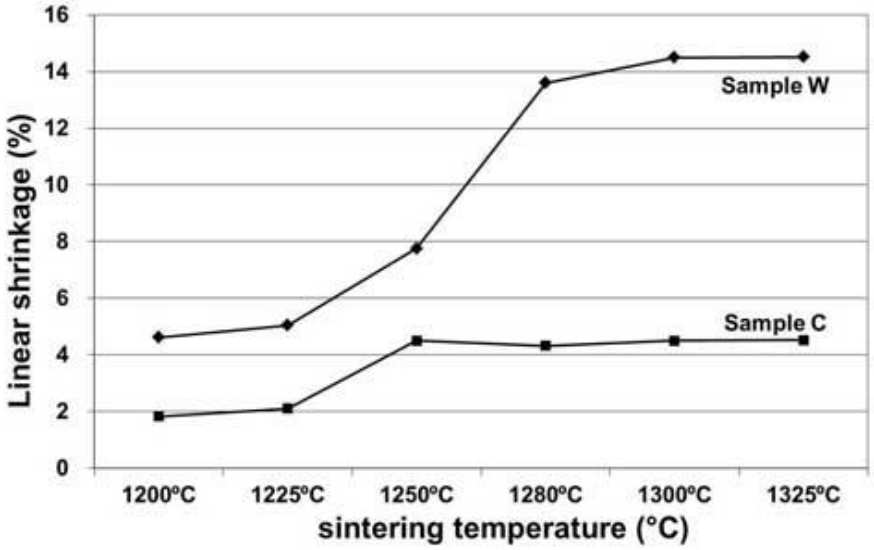

Figure. 5.29 The linear firing shrinkage of the samples W and C after firing at 1200-1325°C.

Water absorption values of samples W and C from 1200°C to 1325°C were shown in Figure 5.30. All W-samples depicted lower values than those of C-samples. Same as the linear firing shrinkage, the Aw of the smaller particle size with CaO, MgO, Fe_2O_3 and ZnO compared to commercial alumina, could be fused at lower temperature and imparted better packing at the same sintering temperature. Moreover, the water absorption values of both samples W and C were constant from 1200°C to 1225°C. The observed values then decreased significantly at 1250°C and remained constant thereafter. The onset temperature was the same as that of the linear firing shrinkage temperature. The findings provided information of the crystalline phase transformation, which will be discussed later.

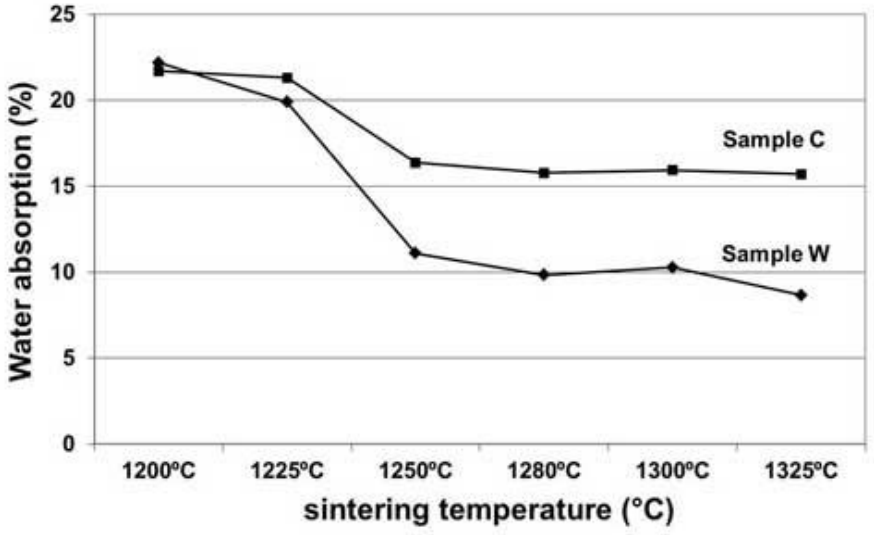

Figure 5.30 Water absorption of the samples W and C after firing at 1200-1325°C.

Figure 5.31 and 5.32 show XRD patterns of samples C and W at all sintering temperatures of 1200-1325 °C. Phase information was compiled in Table 5.13. At 1200°C firing temperature, the sample C consisted of corundum as major phase with minor phases of cristobalite, spinel, mullite, and cordierite. According to Dasgupta and Kumar [18], at the temperature, the corundum phase was formed by the reaction between intermediate phase and cristobalite or amorphous silica. These phases remained the same to 1225°C. At 1250°C, cordierite becomes major phase with minor phases of cristobalite, corundum, spinel, and mullite. As the sintering temperatures increased during 1280-1325 °C, the amount of cordierite increased whereas cristobalite disappeared from the diffraction patterns.

Sintered at 1200°C, sample W obtained spinel as major phase and mullite, corundum and cordierite as minor phases. At 1225°C, spinel still appeared as major phase with an increasing of cordierite. From 1250°C to 1325°C, cordierite became major phase and arose continuously as temperatures increased, whereas the diffracted peak intensities of spinel and mullite obviously decreased. Evidently, cordierite can be obtained in large quantity at low temperatures due to some existing active fluxing agents such as CaO, MgO, Fe_2O_3, and ZnO [19-22] at higher concentrations in both samples C and W. In addition, in comparison with the sample C at the same sintering temperature, the sample W with smaller sized particles having higher surface areas and larger amount of fluxing agents tended to result in larger quantity of cordierite showing in higher proportional to the integrated area intensities obtained from the XRD patterns. Smaller particles, in general, can help pack particles closer during compacting, fuse easier during sintering and hence together with the fluxing agents, synthesize more cordierite that later lowers water absorption but increases linear firing shrinkage.

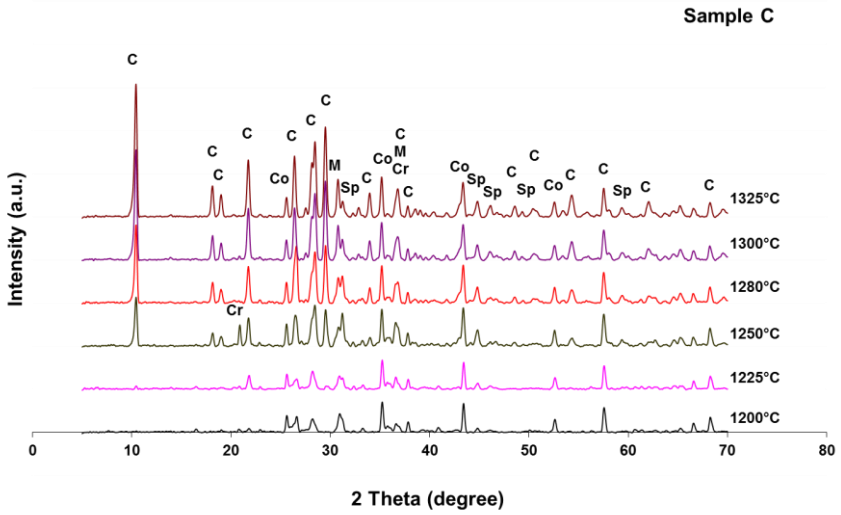

Figure 5.31 XRD patterns of samples C sintered at 1200-1325 °C. The marks are the standard peak positions of Cordierite (C), Spinel (Sp), Cristobalite (Cr), Corundum (Co) and Mullite (M).

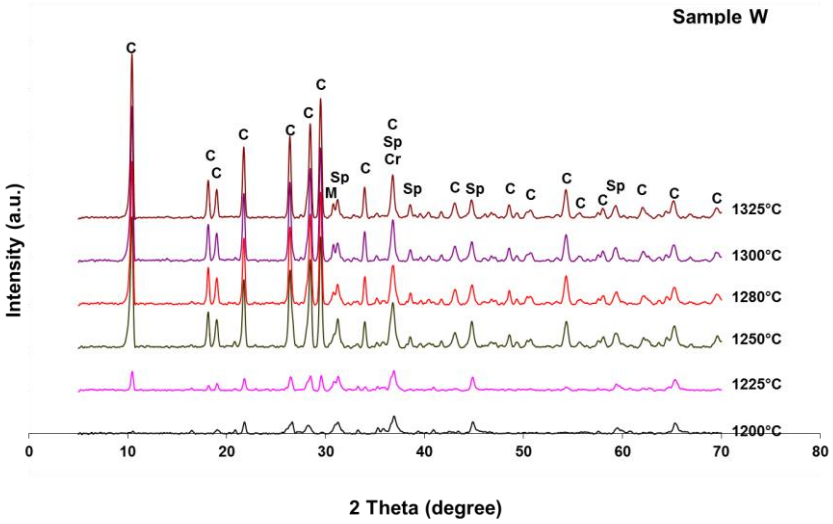

Figure 5.32 XRD patterns of samples W sintered at 1200-1325 °C. The marks are the standard peak positions of Cordierite (C), Spinel (Sp), Cristobalite (Cr), Corundum (Co) and Mullite (M).

Table 5.13 XRD results of sintered samples at various temperatures

Sample	Sintering temperature, (°C)	Main Phase	Other Phases	Integrated Area Intensity of Main Phase
C-1	1200°C	**Corundum**	Cristobalite, Spinel, Mullite, Cordierite	88.436
C-2	1225°C	**Corundum**	Cristobalite, Spinel, Mullite, Cordierite	81.749
C-3	1250°C	**Cordierite**	Cristobalite, Corundum, Spinel, Mullite	168.326
C-4	1280°C	**Cordierite**	Corundum, Spinel, Mullite	259.846
C-5	1300°C	**Cordierite**	Corundum, Spinel, Mullite	351.532
C-6	1325°C	**Cordierite**	Corundum, Spinel, Mullite	436.757
W-1	1200°C	**Spinel**	Mullite, Corundum, Cordierite	111.151
W-2	1225°C	**Spinel**	Mullite, Cordierite	80.088
W-3	1250°C	**Cordierite**	Spinel, Mullite	382.332
W-4	1280°C	**Cordierite**	Spinel, Mullite	390.893
W-5	1300°C	**Cordierite**	Spinel, Mullite	510.360
W-6	1325°C	**Cordierite**	Spinel, Mullite	509.205

COE values of W and C samples decreased with the increasing of sintering temperatures as shown in Figure 5.33. The values were lower for W-sample at all temperatures. At 1225°C, the COE values of both W and C samples dropped distinctly. The COE of sample C decreased from 8.30×10^{-6} °C^{-1} to 5.88×10^{-6} °C^{-1} as the sintering

temperatures increased from 1200°C to 1280°C. The values slightly decreased thereafter and reached the value of 4.98 x 10^{-6}°C^{-1} at the sintering temperature of 1325°C. On the other hand, the COE values of samples W dropped distinctly from 7.35×10^{-6} °C^{-1} (fired at 1200°C) to 4.89×10^{-6} °C^{-1} (fired at 1250°C) and decreased very slightly to reach 3.95 x 10^{-6}°C^{-1} for the highest sintering temperature of 1325°C.

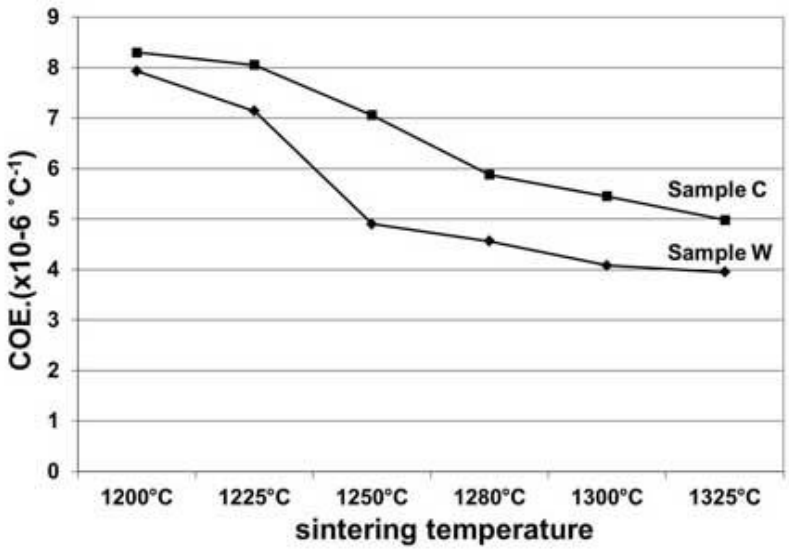

Figure 5.33 COE graph of samples C and W.

Properties of the synthesis bodies W or prototype5 and C were summarized in the Table 5.14.

Table 5.14 Summary of physical properties of the samples at 1325°C

Sample no.	Shock Resistance (°C)	Water Absorption (%)	Firing Shrinkage (%)	Crystalline phase	COE (x10^{-6} °C^{-1})
C-1	290	21.71	1.83	**Corundum** , Cristobalite, Spinel, Mullite, Cordierite	8.3
C-2	290	21.32	2.11	**Corundum** , Cristobalite, Spinel, Mullite, Cordierite	8.05
C-3	290	16.38	4.5	**Cordierite** , Cristobalite, Corundum, Spinel, Mullite	7.06
C-4	290	15.77	4.32	**Cordierite** , Corundum, Spinel, Mullite	5.88
C-5	290	15.93	4.5	**Cordierite** , Corundum, Spinel, Mullite	5.45
C-6	290	15.71	4.52	**Cordierite** , Corundum, Spinel, Mullite	4.98

Table 5.14 Summary of physical properties of the samples at 1325°C (Ext.)

Sample no.	Shock Resistance (°C)	Water Absorption (%)	Firing Shrinkage (%)	Crystalline phase	COE ($x10^{-6}$ $^{\circ}C^{-1}$)
W-1	290	22.19	4.62	**Spinel** , Mullite, Corundum, Cordierite	7.93
W-2	290	19.9	5.04	**Spinel** , Mullite, Cordierite	7.14
W-3	290	11.1	7.76	**Cordierite** , Spinel, Mullite	4.9
W-4	290	9.83	13.6	**Cordierite** , Spinel, Mullite	4.56
W-5	290	10.27	14.5	**Cordierite** , Spinel, Mullite	4.08
W-6	290	8.67	14.52	**Cordierite** , Spinel, Mullite	3.95

It can be deduced from the results that the sintering temperatures increased, the COE decreased as the amount of cordierite increased and the amount of the porosity decreased. The findings seemed to be inconsistent with an equation of coefficient of thermal expansion of composite materials in that the COE had a direct relationship with the amount of cordierite and had an inverse relationship with the amount of the porosity [3, 28, 29]. From the equation (1), the COE was proportional to the volume fraction of materials in the composite. Cordierite was one of the materials which, among all materials, possessed the smallest value of COE (Table 5.11). The only conditions that would, then, lower the COE of the composite is an increasing of the amount of cordierite. The conditions were confirmed by the results from X-ray diffraction (Figure. 5.31, 5.32 and Table 5.12).

Moreover, equation (1) also presented that COE was inversely proportional to the amount of porosity. Figure 5.30 showed that the water absorption values decreased as the sintering temperatures increased which should result in increasing of COE. Instead, the COE values were decreased. The findings implied that the bodies were taken to the verification point, became glassy, and deformed [9]. In addition, the effect of porosity on the COE was surpassed by the excessive amount of cordierite which entailed decreasing of the COE.

In sample C, SEM showed homogeneous structure of fused, recrystallized features and pores in the matrix, Figure 5.34 (A.). EDS analysis and detailed microstructures ofcorundum cordierite and spinel are given in Figure 5.34 B, C and D. SEM micrographs of sample W also shows the fused, recrystallized features and pores in the matrix, Figure 5.35 (A.). EDS analysis and SEM in Figure 5.35 (B.) clearly shows crystal structure of cordierite. The more detailed microstructure of cordierite and spinel are presented in Figure 5.35.(C and D.). Cordierite crystals were clearly observed in sample W which probably due to evolution of flux contained in the body.

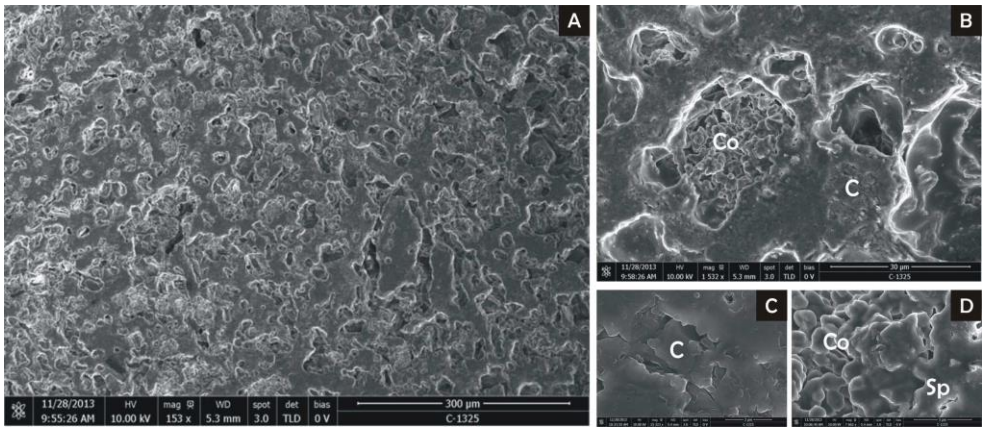

Figure 5.34 SEM micrographs of samples C sintered at 1325°C (A) The etching surfaces by HF 0.1 %, (B) Crystal structure of cordierite and corundum, (C) Crystal structure of cordierite, (D) Crystal structure of corundum. (cordierite:Co, corundum:C, spinel:sp).

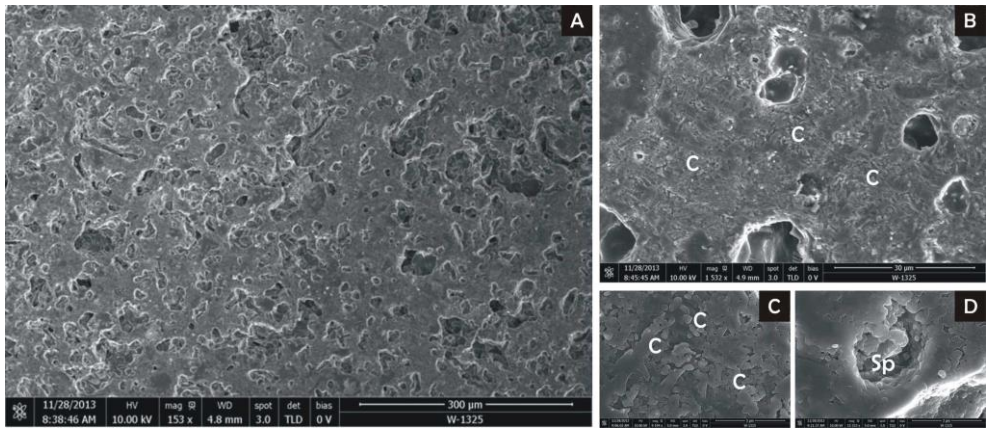

Figure. 5.35 SEM micrographs of samples W sintered at 1325°C (A) The etching surfaces by HF 0.1 %, (B) Crystal structure of cordierite, (C) Crystal structure of cordierite, (D) Crystal structure of spinel. (cordierite: C, spinel: sp).

จากการศึกษาผู้วิจัยได้พบปัญหาบางประการที่จะเป็นประโยชน์สำหรับผู้สนใจในการวิจัยในอนาคตโดยสรุปสภาพปัญหาและข้อเสนอแนะแยกเป็นประเด็นต่างๆ ดังนี้

1. Raw material, จากข้อมูลของผู้ประกอบการด้านการจัดหาวัตถุดิบตั้งต้น พบว่า Product specification ที่ผู้ประกอบการให้แก้ผู้ซื้อจะมีแค่ Chemical composition และ ค่า Physical appearance บางค่า เช่น ขนาดผ่านตะแกรงร่อน (mesh) เป็นต้น แต่ค่าที่มีความเฉพาะเจาะจงผู้ประกอบการจะไม่ได้มีข้อมูลให้ เช่น ค่าสัมประสิทธิ์การขยายตัวเมื่อร้อน (COE) ของวัตถุดิบ ซึ่งมีความสำคัญกับงานวิจัยชิ้นนี้ ค่า COE ของวัตถุดิบตั้งต้นจะมีผลทำให้สมบัติของชิ้นงานต้นแบบ มีค่าการต้านทานการเปลี่ยนแปลงอุณหภูมิอย่างฉับพลันต่ำตามไปด้วย as equation1. p.55

2. Particle size distributions, ในงานวิจัยชิ้นนี้ผู้วิจัยไม่ได้หาค่าของ raw material partaicle size distributions เนื่องจากข้อจำกัดด้านเครื่องมือ แต่พบว่าเวลาในการบดเพิ่มขึ้นจะทำให้ขนาด partaicle size เล็กลง ซึ่งจะมีผลต่อ physical property ในด้าน การหลอมตัวที่ดีขึ้นในอุณหภูมิที่ต่ำลง, water absorption value decreased, Linear firing shrinkage tentatively increased, COE decreased and increased cordierite Intensity. เมื่อประกอบกับการเลือกวัตถุดิบตั้งตนที่มีค่า COE ต่ำ จะทำให้ความจำเป็นในการเติม spodumene เพื่อลด COE ของเนื้อดินลดลง

3. Raw material from waste, แทนการทำเหมืองแร่ เพราะยังมีอีกหลายอุตสาหกรรมที่มีขยะเหลือทิ้งจากการผลิตที่มีความเป็นไปได้ในการนำกลับมาใช้ใหม่เพื่อให้ได้ประโยชน์สูงสุด